In Situ Cloud Sensing with Multiple Scattering Lidar: Design and Validation of an Airborne Sensor

K. FRANKLIN EVANS

Program in Atmospheric and Oceanic Sciences, University of Colorado, Boulder, Colorado

DARREN O'CONNOR, PAT ZMARZLY, AND R. PAUL LAWSON

SPEC Inc., Boulder, Colorado

(Manuscript received 10 October 2005, in final form 30 December 2005)

ABSTRACT

The in situ cloud lidar is designed to measure cloud volumes of millions of cubic meters to overcome the sampling limitations of traditional cloud probes in inhomogeneous clouds. This technique sends laser pulses horizontally from an aircraft inside an optically thick cloud and measures the time series of the multiply scattered light with wide field-of-view detectors viewing upward and downward. The extinction in liquid clouds averaged over tens to hundreds of meters and the distance to cloud boundaries can be retrieved from the signal measured by a single-wavelength in situ lidar. This paper describes the design and operation of an in situ cloud lidar. A laser in the aircraft cabin outputs 532-nm wavelength pulses at 10 Hz, which are sent through beam-expanding optics for eye safety. The upward- and downward-viewing detectors use photomultiplier tubes and operate with either daytime (3° half angle; 0.37-nm solar-blocking filter) or nighttime (30°) optics. Example daytime lidar signals in dense cloud have a dynamic range of 1000 after solar background subtraction. Results from a nighttime flight in marine stratus are analyzed in detail. The variations in the lidar signals with aircraft travel are much smoother for the longer photon travel times, indicating that the later times sample volumes hundreds of meters in size. Extinction retrievals for 25-m-radius volumes have high correlation ($R^2 = 0.84$) with Forward Scattering Spectrometer Probe (FSSP)-derived extinction, while the correlation is relatively low ($R^2 = 0.40$) for 200-m volumes due to cloud inhomogeneity. Lidar retrievals of cloud-base and -top height from inside the cloud are consistent with cloud boundaries obtained from aircraft penetrations on ascents and descents.

1. Introduction

Traditional in situ cloud probes, whether of the particle-counting or imaging variety, sample very small volumes compared to the whole volume of the clouds being measured. For example, the Particle Measuring Systems (PMS) Forward Scattering Spectrometer Probe (FSSP)-100 probe (Knollenberg 1981) samples roughly 50 $cm^3\,s^{-1}$ on a 100 $m\,s^{-1}$ aircraft. The small sampling volumes of these probes prevent the measurements from being representative of larger scales due to the inhomogeneities prevalent in clouds. An accurate in situ cloud measurement technique that samples a volume having a radius of hundreds of meters would be valuable for cloud microphysical and radiative transfer research, and especially for validation of satellite cloud remote sensing techniques.

The in situ cloud lidar technique (Evans et al. 2003) measures water cloud extinction at scales of tens to hundreds of meters (volumes of 10^6 to 10^9 m^3). The laser beam exits the aircraft horizontally, while very wide field-of-view detectors view upward and downward. Inside optically thick clouds the laser pulse is multiply scattered by cloud droplets, and a small portion of the light returns to be measured by the detectors. The signal measured by the instrument is the number of photons returned as a function of photon travel time for each detector. The lidar return shape and amplitude contain information about the distance to the cloud boundaries and the volume-average extinction at different spatial scales around the instrument.

Other multiple-scattering-based lidar cloud remote

Corresponding author address: Dr. K. Franklin Evans, University of Colorado, 311 UCB, Boulder, CO 80309-0311.
E-mail: evans@nit.colorado.edu

sensing techniques have been developed recently. For optically thick clouds the "off-beam" lidar technique has been proposed to remotely sense both optical depth and geometric thickness of a cloud layer (Davis et al. 1999). A ground-based wide angle imaging lidar (Love et al. 2001) built at Los Alamos National Laboratory measured optical depth and cloud thickness in March 2002 (Polonsky et al. 2005). An aircraft-based instrument, Thickness from Offbeam Returns (THOR), built at the National Aeronautics and Space Administration (NASA) Goddard Space Flight Center, successfully operated on its first test flight in March 2002 (Cahalan et al. 2005). Both the off-beam lidar technique and the in situ lidar technique take advantage of multiple scattering and photon diffusion to retrieve properties over large cloud volumes.

The previous work on the in situ lidar (Evans et al. 2003) was mainly theoretical. Diffusion theory calculations showed that the expected in situ lidar time series depends strongly on the extinction and has a functional form of a power law times an exponential, with the exponential scale depending on the distance to the cloud boundary. Simulations of 532-nm wavelength in situ lidar time series were made with a Monte Carlo radiative transfer model in stochastically generated inhomogeneous stratus clouds. Retrieval simulations predicted that 1) extinction at four Gaussian volume-averaging scales (rms radii from 25 to 200 m) could be retrieved with about 7% rms accuracy, 2) optical depth at area-averaging scales from 50 to 400 m could be retrieved to about 12%, and 3) cloud geometric thickness over the range 200–1000 m could be retrieved to 60 m. Simulations of a proposed dual-wavelength lidar (532 and 1550 nm) indicated good accuracy for liquid water content and effective radius retrievals. A mountaintop laboratory demonstration of the in situ lidar technique validated the expected power-law time series behavior.

With NASA Small Business Innovative Research funding, SPEC, Inc. designed, built, and tested a single-wavelength in situ cloud lidar on a research aircraft flown in marine stratus. The next section of this paper describes the design and operation of the in situ lidar. Section 3 describes the successful nighttime science flight and shows lidar data from daytime and nighttime operation in liquid clouds. Section 4 briefly describes the retrieval method, compares lidar retrieved extinction with FSSP-derived extinction, and compares lidar retrieved cloud-top and -base altitude with those derived from aircraft penetrations. The last section summarizes the results and discusses possibilities for future development of the in situ lidar technique.

2. In situ lidar design and operation

The in situ cloud lidar consists of 1) a laser in the aircraft cabin that sends light pulses horizontally through an optical flat installed in a cabin window, 2) a detector and electronics module mounted on the leading portion of the wing-tip tank, and 3) a data system computer in the aircraft cabin (Fig. 1). The two detectors view up and down from the sensor head in front of the wing-tip tank. Each detector collects the scattered light with either wide field-of-view (nighttime) optics or narrow field-of-view (daytime) optics. The photomultiplier tube (PMT) in each detector is controlled and its output current measured by a dedicated electronics board. The two electronics boards and power supply fit in a PMS canister inside the wing-tip tank. The characteristics of the in situ lidar are quantified in Table 1.

a. Laser and detector optics

The laser source used for the in situ lidar is a New Wave Research model Tempest-300–532 frequency doubled Nd:YAG laser operating at 532 nm with an output pulse energy of 182 mJ, pulse width of 5 ns, and a repetition rate of 10 Hz. The output beam from the laser is expanded using a Galilean-type beam expander to introduce a half-angle divergence of 0.5° for eye safety considerations. The laser beam exits the aircraft horizontally on the starboard side. The SPEC research aircraft has been modified with an Federal Aviation Administration (FAA)-approved optical quality window to maximize laser transmission. The system is designed to operate within the critical visual interference level of 1.25×10^{-6} J cm^{-2} as defined in ANSI Z136.6–2000, which defines safety guidelines for using lasers outdoors. The above exposure limit is at a horizontal distance of 1000 ft from the moving aircraft, a very conservative horizontal separation distance for an aircraft in flight. The laser is not operated while the aircraft is in a banking turn low to the ground.

The design for the detector collection optics utilizes two different approaches for daytime and nighttime operation. Figure 2 shows the basic elements for each system. The daytime optics configuration uses a narrow bandwidth interference filter (0.37-nm half-power width) operating over a half angle of approximately 3° to minimize the incoming solar background. A collection lens with an approximately 50-mm-diameter aperture is used in combination with a field stop to match the field of view of the daytime optics to the angular response of the filter. The filter is temperature controlled to 0.25°C to maintain a constant peak transmission over a range of flight temperatures. An electronically controlled shutter is used to block sunlight from

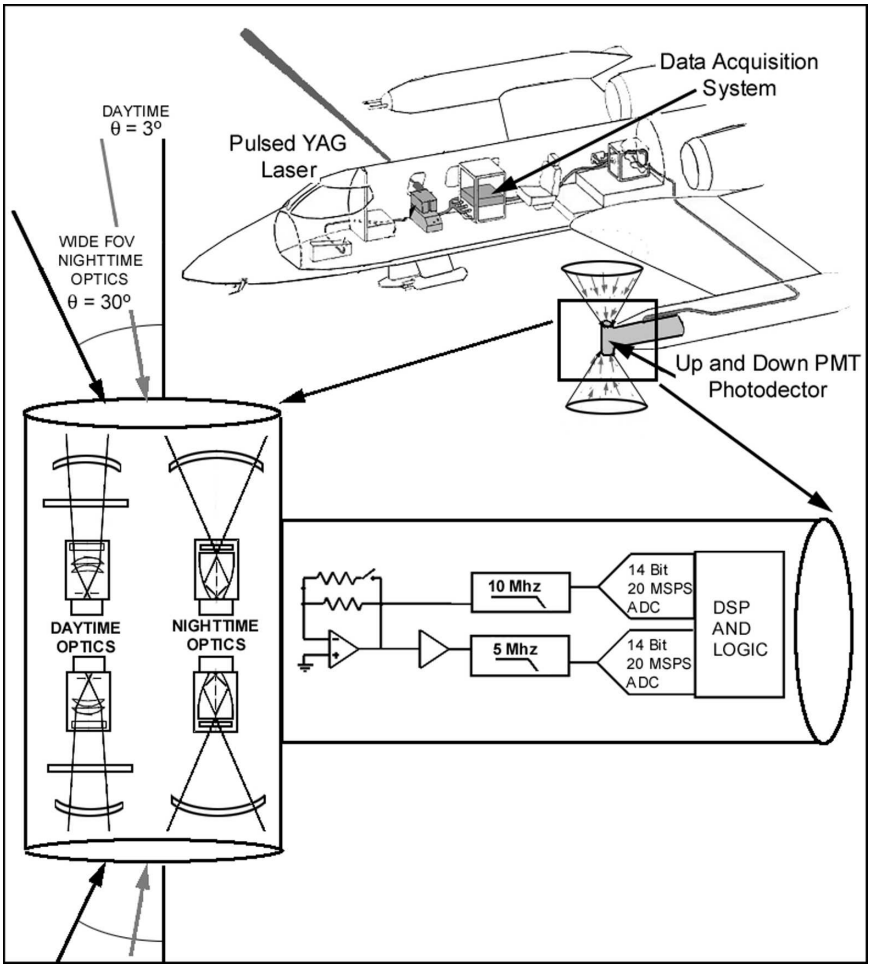

FIG. 1. A schematic diagram of the in situ cloud lidar system.

reaching the PMT when the lidar system is not operating. A quartz window is used to provide optical access for the detector while maintaining a dry, hermetically sealed environment at flight altitudes up to 40 000 ft.

TABLE 1. In situ lidar characteristics.

Laser pulse energy	182 mJ
Wavelength	532 nm
Pulse rate	10 Hz
Beam divergence	0.5° (half angle) with beam expander
No. of detectors	2 (upward and downward viewing)
Detector aperture	50-mm diameter
Detector field of view	30° half angle (nighttime optics) 2.8° half angle (daytime optics)
Background filter width	77 nm at half max (nighttime optics) 0.37 nm (daytime optics)
ADC sample time	50 and 100 ns
Electronics dynamic range	10^6 with three amplifier stages and 14-bit ADC

The nighttime optics configuration uses a wide bandwidth interference filter (77-nm half-power width) and a compound parabolic concentrator (CPC) (Welford and Winston 1989) to maximize the collection of scattered photons in the absence of a solar background. A CPC is a nonimaging optical element that collects rays entering within a specific angular range and rejects incoming rays at larger angles. In our case, the CPC collects incoming photons at a half angle up to 30° over an aperture of approximately 50-mm diameter. The photons exit the CPC at angles approaching 90° before being collected by the 25-mm-diameter PMT. The CPC is used to maximize the etendue (the product of solid angle and area) of the collection system within the limited space available that would otherwise not be easily achieved with a conventional optical system. Each CPC was manufactured from 6061-T6 aluminum on a single-point diamond-turning computerized numerically controlled (CNC) machine.

The airborne detector module, with the upward- and

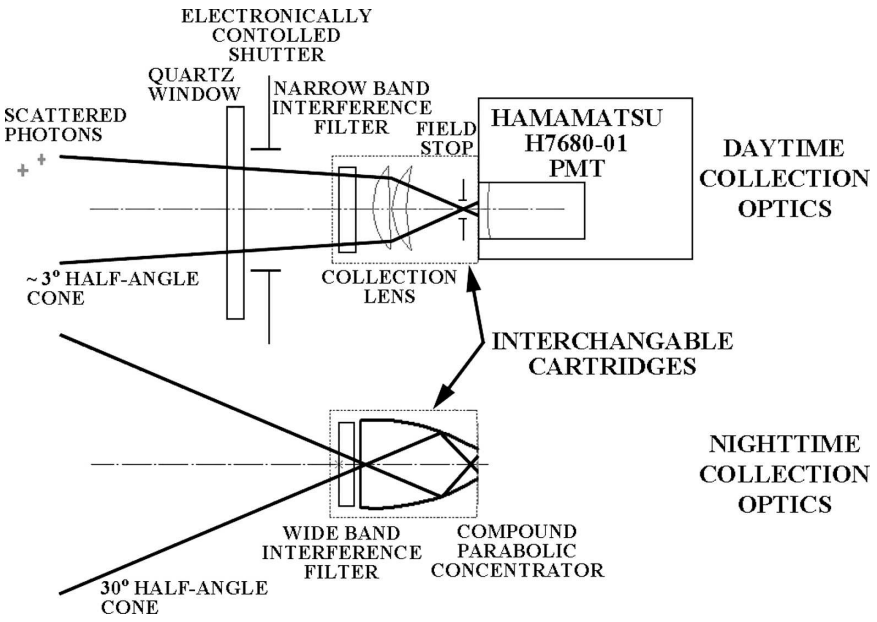

FIG. 2. Daytime and nighttime collection optics systems. The daytime configuration uses a narrow FOV to reject the solar background. The nighttime configuration uses a compound parabolic concentrator to maximize the FOV and the collection of scattered photons in the absence of a solar background. The components are housed in interchangeable cartridges that can be manually changed before flight.

downward-looking detectors, is a pressurized, insulated, and temperature-controlled vessel. Each PMT detector has a set of daytime and nighttime optics. The daytime and nighttime collection optics are packaged in cylindrical cartridges that are nearly identical in size and mounted to a carousel that can be manually rotated to select the desired configuration before takeoff. Figure 3 is a solid model of the detector assembly illustrating the relative location of the upward and downward PMT and their respective collection optics cartridges.

The optical response for each collection optics configuration has been estimated using a combination of laboratory measurements and ray tracing analysis. The angular response for photons hitting the PMT is relatively flat up to incident angles of approximately 20°. Because photons can leave the CPC at angles up to 90°, it was necessary to evaluate the response of the PMT to incident photons at these large angles. The angular response of the PMT was measured in the laboratory. Each of the interference filters used in the daytime and nighttime optical configurations has an angular dependent transmission that was measured by the manufacturer. For the daytime configuration, the measured response of the narrowband interference filter and PMT were input into an optical design program and combined with the quartz window, collection lens, field stop, and other appropriate limiting apertures such as the electronic shutter. Rays were traced through the system at various field angles and the angular dependent transmission of the system was calculated. For the nighttime configuration, the narrowband filter, the collection lens, and the field stop were replaced with the CPC and the measured response of the appropriate wideband interference filter.

b. Electronics

The in situ lidar electronics processes 10-Hz samples of in cloud photon returns. Each return begins with the laser system sending out a timing signal, QSYNC, indicating that the 5-ns pulse will occur 100 ns from QSYNC's rising edge. The electronics' digital control system then uses user-selected parameters to decide when to turn on the photon-sensing analog system. It also controls how many samples to take at a fast sample interval of 50 ns before switching to a slower sample interval of 100 ns. A user-selectable number of samples are taken from each detector for each laser pulse and transmitted over an RS-422 channel at 480 kbps to a data system computer. The two detector electronics are operated independently, with control of abovementioned parameters, as well as gain settings and operating temperatures of system components offered via the data system interface. The resulting individual photon return events are displayed on the computer monitor, a depiction of which is shown in Fig. 1. The monitor in the figure shows a single channel's low-gain channel

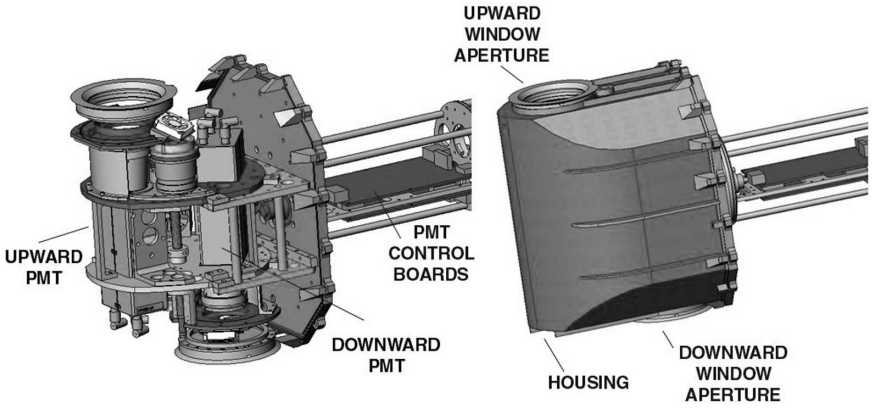

FIG. 3. Airborne detector assembly showing locations of upward- and downward-looking PMTs and location of interchangeable cartridges to select between daytime and nighttime optical configurations.

(light gray) plot flattening out shortly after the high-gain channel (black) becomes active and is representative of real photon return events.

The electronics system for each in situ lidar detector consists of a photomultiplier tube system; a switched transimpedance amplifier (TIA) and a second stage gain amplifier; lowpass filters feeding a pair of high-speed analog-to-digital converters (ADC); and a digital signal processor (DSP) and control logic. These components are outlined in Fig. 1. The PMT module, a Hamamatsu H7680-1, includes a voltage programmable high-voltage power supply, which allows the PMT high voltage to be gated off for a programmable period during the initial photon return to avoid saturation. As shown in Fig. 1, there are low- and high-gain channels for each detector. The second stage amplifier (high-gain channel) is sampled at a slower rate, as during the latter period of a photon return event when changes in photon return rate become much slower.

The switched resistor in the TIA feedback effectively provides two gain settings for the two channels, but with the improved signal-to-noise ratio offered by putting more gain in the first stage amplifier. The switch is opened, yielding a larger TIA gain, during the latter portion of the photon return event. The photon return threshold at which the TIA gain switches is programmable via the data system. The first stage gain then goes up by a factor equal to the value of gain of the second amplifier. This effectively produces a smoothly measured signal with the two channels, each with low (initial photon return) and high (subsequent photon return) gain settings. There is some overlap between the two gain channel's measurement range, both before and after the TIA gain switch occurs, providing a consistent measurement.

The dynamic range of the electronics (range of the largest to the to smallest measurable PMT current) is estimated from $D = G_1G_2C_{\max}/C_{\min} = 46.4 \times 46.4 \times 16384/34 = 1.0 \times 10^6$, where G_2 is the gain of the second stage amplifier, G_1 is the effective gain from switching out the first stage resistance, and $C_{\max}/C_{\min}$ is the ratio of the maximum to minimum ADC counts; $C_{\min} = 34$ was chosen because the discretization error to the measured signal is less than 3%, and the gains of 46.4 were chosen to optimize the dynamic range and signal-to-noise ratios. The instrument has in fact measured signals with a dynamic range greater than the above prediction. Since the in situ lidar also benefits from averaging together of samples late in the photon return event, the lower limit to $C_{\min}$ can approach a value of 1 count, for which the dynamic range predicted is 3.5×10^7.

To produce the optimum PMT current over the large range of cloud extinction, the DSP logic implements an automatic gain control system for the PMT gain. When the peak PMT current exceeds a preset threshold, the DSP lowers the PMT gain by a factor of 10; when the current is below another threshold, the DSP raises the PMT gain by a factor of 10. There is hysteresis built in to the thresholds, and the DSP performs the amplitude check once every third laser pulse. This combination was found to maximize the dynamic range of individual laser pulse measurements by appropriately setting the PMT gain to the ambient cloud conditions in real time, while limiting the frequency of changes to the gain that would otherwise degrade the measurement.

c. Calibration

The in situ lidar is calibrated with the "system equation" approach, which attempts to use measured values for each portion of the system, from the laser power to the PMT detector gain. This approach is less accurate

than a proper experimental calibration, but is simpler and adequate for this initial in situ lidar experiment. The desired output of the calibration is the "photon fraction," which is the fraction of emitted photons that returns to the detector aperture per area per solid angle per time. The calibration starts by converting the ADC counts to voltages and hence to PMT output current using the TIA feedback resistances for each gain stage. The PMT current is then converted to photon fraction $p(t)$ using

$$p(t) = \frac{I_{\mathrm{PMT}}(t)}{qG_{\mathrm{PMT}}A_{\mathrm{det}}\Omega_{\mathrm{det}}(E_l\lambda/hc)}, \quad (1)$$

where $I_{\mathrm{PMT}}(t)$ is the PMT output current, q is the charge on an electron, G_{PMT} is the PMT gain in output electrons per incident photon (includes the quantum efficiency), A_{det} is the active area of the detector aperture, Ω_{det} is the effective solid angle of the detector (including the optics transmission), and $E_l\lambda/hc$ is the number of photons output by the laser pulse with energy E_l operating at wavelength λ. Here G_{PMT} is parameterized as a function of PMT control voltage V by $G_{\mathrm{PMT}} = \exp[g_1 + g_2 \ln(V) + g_3 \ln(V)^2]$; Ω_{det} is derived by integrating the detector angular response function over angle. The laser output energy $E_l = 182.2$ J was measured by the manufacturer.

The gain curve for the down detector PMT was measured by the manufacturer, but the other PMT was not measured. Using the same PMT gain curve for the up detector resulted in noticeable jumps in photon fraction between laser shots before and after PMT gain changes. The size of the jumps among the lowest three PMT gain settings, which are the relevant ones inside cloud, were used to adjust the PMT gain curve for the up detector. The PMT gain of the up detector relative to the down detector was determined by requiring the photon fraction at 0.5 μs in the densest cloud to have the same value for the up and down detectors.

3. In situ lidar deployments

The lidar was deployed on three engineering flights in November 2004 to test the instrument operations. Several adjustments were made to the operations of the electronics based on problems noted. We report on results from one engineering flight to illustrate daytime operation of the in situ lidar.

a. Daytime engineering flight example

The first engineering flight was taken on 3 November 2004, and lidar returns in liquid cloud were obtained over southern Oklahoma. Figure 4 shows an example

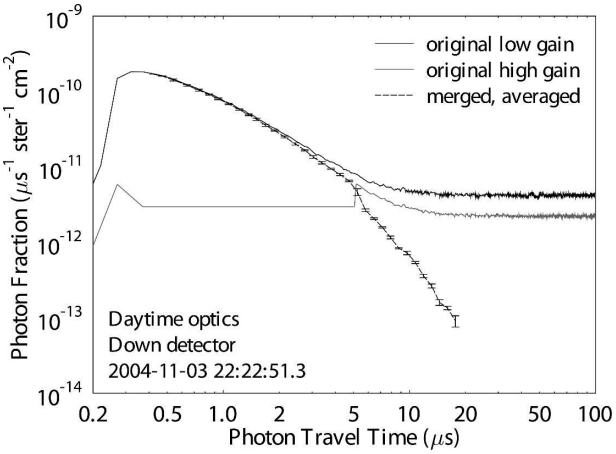

FIG. 4. An example lidar signal in dense cloud on the first engineering flight. The calibrated lidar data from the low- and high-gain channels are shown with solid lines. The dashed line shows the data from the two channels merged and averaged over log-spaced time bins and with the solar background signal subtracted. The error bars show the standard error of the photon fraction from the variability in each time bin.

signal from one laser shot in thick cloud. The first part of the signal is obtained from the low-gain channel while the high-gain channel is saturated. The high-gain channel is then used for the latter part of the signal. There is a gap in signal strength between the high- and low-gain channel values around 5 μs due to an amplifier voltage offset, which was subsequently fixed. The average and standard error of the calibrated and merged photon fraction are calculated for time bins spaced logarithmically by a factor of 1.1. This averaging greatly reduces the noise for the latter time bins, which contain many samples, and it also provides an uncertainty estimate. After about 10 μs in this case the signal is dominated by the solar background. The merged and averaged signal also has the solar background subtracted (using the average from 30 to 100 μs).

In this example with the daytime optics, the peak lidar signal is about 40 times above the solar background. With background subtraction the dynamic range is more than three orders of magnitude and the usable signal extends beyond 15 μs. This is a fairly benign situation for solar background, since the solar zenith angle is 76° and the cloud extinction is high. Nevertheless, we expect that daytime in situ lidar retrievals of extinction will be possible in most clouds.

b. Analysis of science flight data

The in situ lidar science flight was flown out of Corpus Christi, Texas, during the evening of 1 December 2004 local time (2 December 2004 UTC). Approxi-

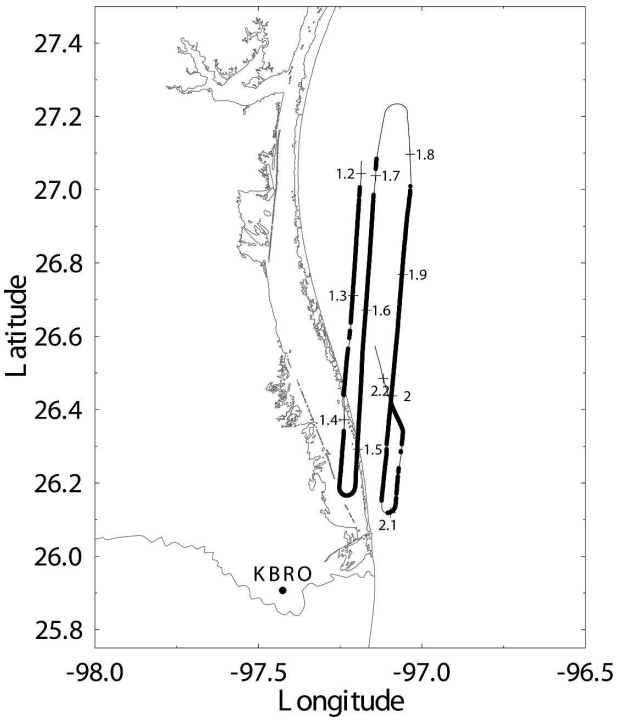

FIG. 5. The path of the cloud portion of the science flight on 2 Dec 2004 UTC off the coast of south Texas. The dots along the line indicate when the aircraft was in cloud as indicated by an FSSP concentration of more than 10 cm^{-3}. The numbers along the flight track are the times in UTC hours. The location of the Brownsville, TX, airport (KBRO) is shown.

mately north–south legs were flown in darkness just off the coast of south Texas (Fig. 5), mostly in cloud for about 1 h. Figure 6 shows the flight altitude varying from about 1000 to 1800 m during this portion of the flight.

The in situ lidar measurements of cloud extinction are compared with extinction derived from the PMS FSSP-100 (Knollenberg 1981) with a Signal Processing Package (SPP-100) electronics upgrade from Droplet Measurement Technologies (DMT). An inspection seven weeks later at DMT showed that the FSSP had a misaligned beam-steering prism, which reduced the nominal 2.7-mm depth of field to about 0.7 mm. A calibration performed at DMT indicated that the FSSP concentration values should be multiplied by a factor of 3.45 (which has been done here), but that the particle sizing was not affected. The FSSP was sampled at 10 Hz, but averaged to 1 Hz. The sample volume of the FSSP-100 with its reduced depth of field is roughly 10^{-5} m^3 s^{-1} at 100 m s^{-1} airspeed.

The aircraft also carried a PMS/Commonwealth Scientific and Industrial Research Organisation (CSIRO) ("King") hot wire liquid water probe, which is used here to check the FSSP calibration. Over all the samples in the analyzed portion of the flight (1.19 to 2.22 h UTC) a linear regression of the FSSP liquid water content (LWC) to the King probe LWC gives $LWC_{FSSP} = 0.0107 + 0.846(LWC_{King})$ with an R^2 correlation of 0.873. This suggests that the correction factor applied to the FSSP data is approximately correct, though perhaps low when compared with the King probe.

To illustrate the thermodynamic environment of the cloud sampled by the in situ lidar, the LWC and temperature are plotted as a function of altitude in Fig. 7. The envelope of LWC points reaches nearly to the adiabatic line of increasing LWC with altitude, which suggests that the cloud layer is well mixed with some nearly adiabatic regions. The FSSP LWC envelope being slightly below the adiabatic LWC may be due to the FSSP depth-of-field correction factor being somewhat too small. The temperature increase above cloud top indicates that the cloud layer is inversion capped. Using surface observer cloud-type definitions, we classify this cloud as stratus because it does not contain individual cloud elements (two legs have continuous cloud over >50 km).

Based on the expected lidar signal from diffusion theory, the function

$$1n p(t) = a - b\ln(t) - ct \qquad (2)$$

is fit to the log time bin-averaged photon fraction signal with a linear least squares procedure. The three fit parameters (a, b, and c), rather than the whole time series, are the inputs to the cloud retrieval (Evans et al. 2003). The photon fraction uncertainty for each time bin is used in the fit, though the uncertainty is not allowed to be less than 0.02. The fits use those time bins between 0.4 and 40 μs for which the photon fraction is greater than 10^{-15} $\mu s^{-1} ster^{-1} cm^{-2}$.

Figure 8 shows example processed lidar signals and functional fits for the up and down detectors for one laser shot. At this point in the flight (1.2714 h UTC) the FSSP cloud extinction of 31 km^{-1} was decreasing from a peak above 75 km^{-1}. Since the aircraft altitude of 1.483 km was near the cloud top, the upward pointing detector signal is lower and decreases more rapidly than the downward detector.

Rarely the lidar signals are grossly in error, apparently due to electronics glitches. These shots are successfully detected and removed with an editing procedure based on the deviation in the a fit parameter from the local values. Shots for which the deviation from a linear regression of the eight surrounding shots exceeds five standard deviations are edited out (unless the absolute deviation is less than 0.1).

Examples of the lidar signal sampled at five selected

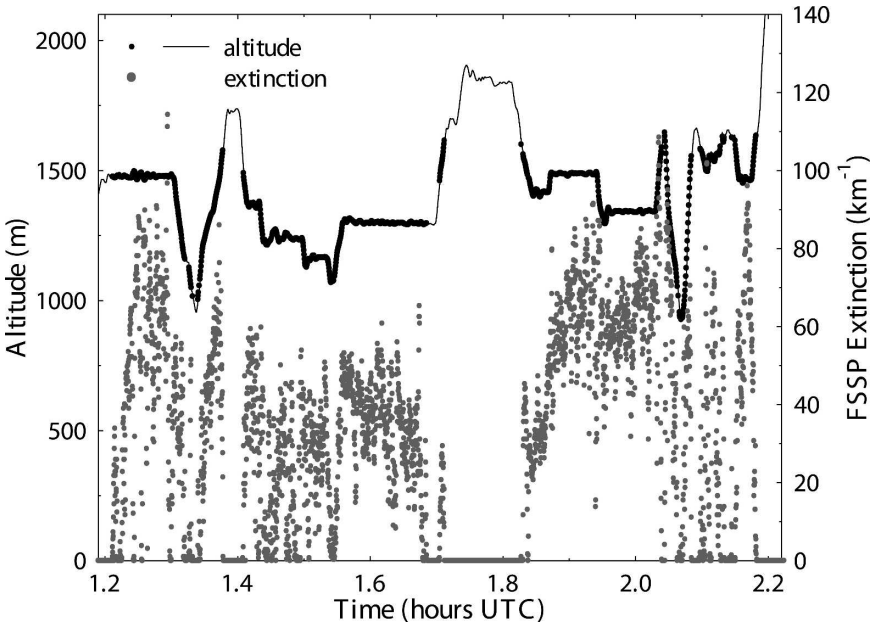

FIG. 6. The aircraft altitude and the FSSP-derived extinction during the flight on 2 Dec 2004 UTC. The dots along the line indicate when the aircraft was in cloud.

photon times as a function of laser shot time are shown in Fig. 9. The signal sampled at later photon times changes much more slowly with the aircraft travel than the signal at shorter photon times, especially for the downward detector. During this level portion of the flight the aircraft is near cloud top, which results in more multiple scattering of the laser light and hence spatial smoothing for the downward-viewing detector as compared to the upward-viewing detector. The smoothing is also more evident in the higher photon

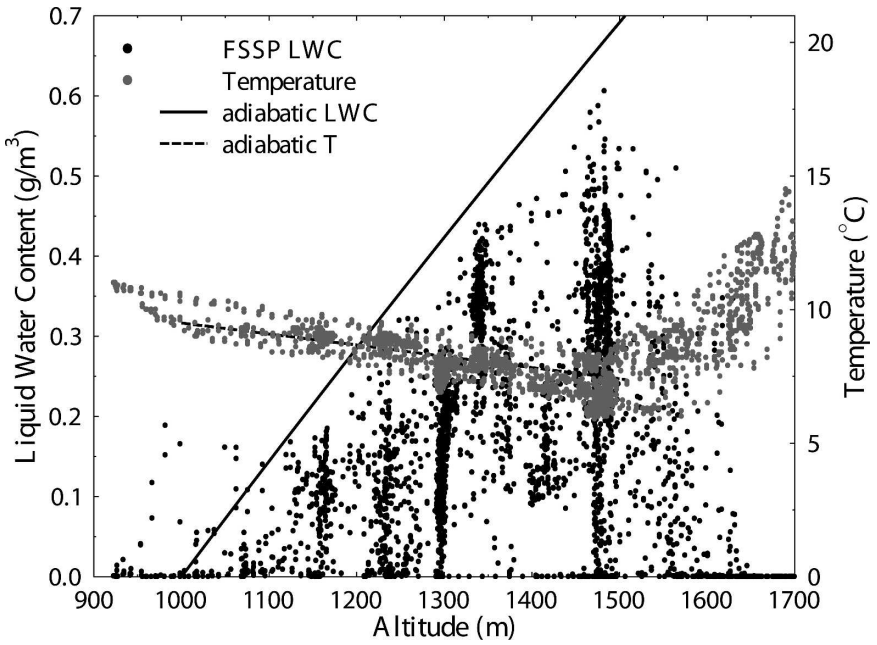

FIG. 7. The FSSP LWC and air temperature as a function of aircraft altitude on the 2 Dec 2004 flight. The adiabatic LWC and temperature lines are calculated assuming cloud base at 1000 m (907 mb and 9.5°C).

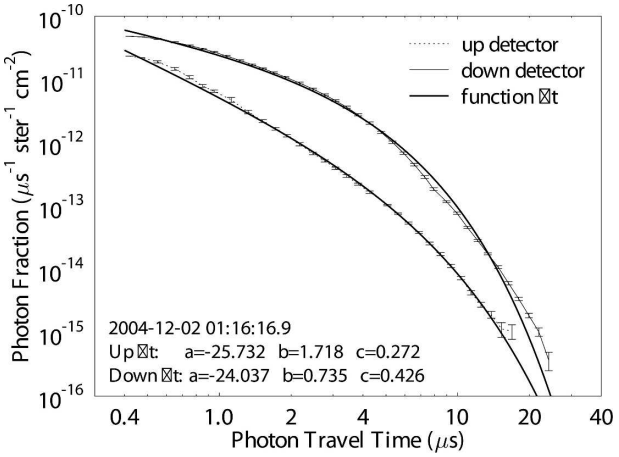

FIG. 8. An example of the calibrated, merged, and time bin averaged lidar signals for up and down detectors from the science flight. The fits of the function $\ln p(t) = a - b \ln(t) - ct$ are shown and the coefficients listed in the legend. The functional fits take into account the error bars on the lidar signals.

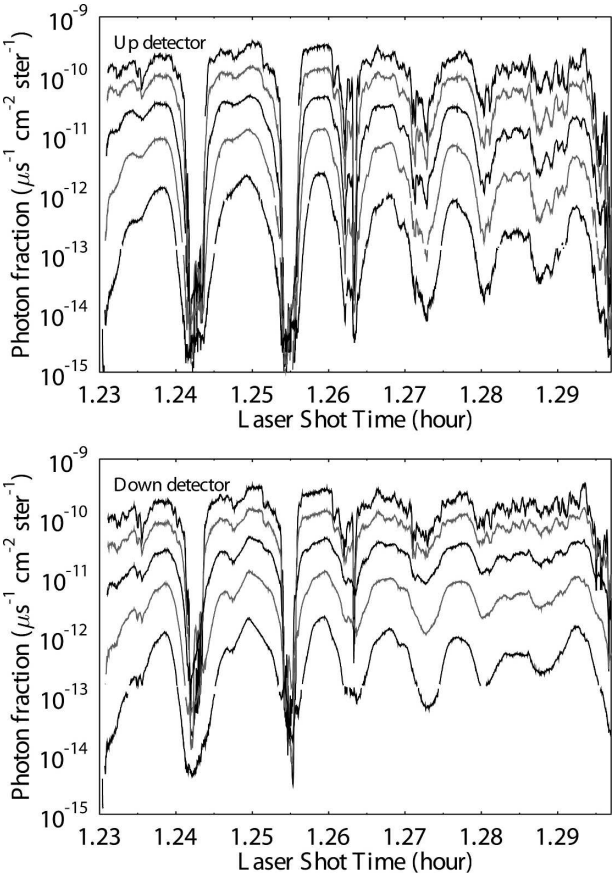

FIG. 9. Examples of the lidar signal at five selected photon times (0.5, 1.0, 2.0, 4.0, and 8.0 μs, from top to bottom in each panel) as a function of laser shot time for the up and down detectors.

fraction, and hence higher extinction, regions. This smoothing of the lidar signal with aircraft distance is closely related to the radiative smoothing concept in remote sensing (e.g., Davis et al. 1997).

How this smoothing behavior depends on the photon time can be quantified with structure function analysis. The normalized structure function for time difference δt is defined by

$$S(\delta t) = \frac{\langle [p(t) - p(t + \delta t)]^2 \rangle}{\mathrm{var}[p(t)]}, \tag{3}$$

where $p(t)$ is the photon fraction, the angle brackets $\langle\rangle$ indicates an average over all valid points with time t, and var$[p(t)]$ is the photon fraction variance. The structure functions are calculated for all of the dense cloud portions of the science flight, which are defined using a photon fraction threshold (varying for each photon time) that results in about 16 300 samples. Based on the number of remaining samples, these thresholds correspond to an FSSP extinction of about 34 km^{-1}. The structure functions are plotted in Fig. 10. The signal for later photon times clearly has much less variability than that for earlier photon times for laser shot times less than about 5 s, or about 500-m spatial scale using the 110 m s^{-1} average aircraft speed. At about 2-km spatial scale (20-s shot time difference) the structure functions of the lidar signals at the different photon times is the same. The radiatively smoothed portion of the structure functions is scaling as shown by the dashed lines. The power-law slope varies from 1.4 for 0.5 μs and 1.0– to 1.7 μs for 8.0 μs. The less steep portion of the later photon time structure functions from 0.1 to 0.3 s is probably from extra variability due to instrument noise. The 0.5-μs structure function clearly has another scaling regime at scales from about 200 to 1000 m (as shown with the dotted line), which is indicative of the true cloud variability.

4. Retrieval and validation

The average cloud extinction (over different size volumes), cloud thickness, and cloud relative aircraft altitude are retrieved from the a, b, and c fit parameters using the approach in Evans et al. (2003). In situ lidar signals for upward- and downward-viewing detectors with nighttime optics are simulated with a Monte Carlo model at 400 locations in 100 stochastic fractal 3D stratus cloud fields. These overcast clouds have partially correlated LWC and droplet number concentration fields and are generated with a wide range of cloud thickness, mean and variability of LWC and concentration, and power spectral slope. The changes from Evans et al. (2003) are that the clouds have a uniform distri-

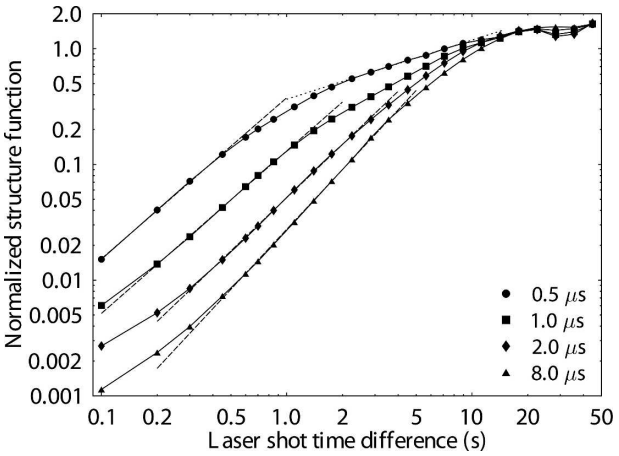

FIG. 10. Structure functions as a function of laser shot time difference for the downward-viewing detector lidar signal sampled at four photon times. The shot time difference may be converted to distance by multiplying by the mean aircraft speed of 110 m s^{-1}. The dashed or dotted lines illustrate the scaling portions of the structure functions.

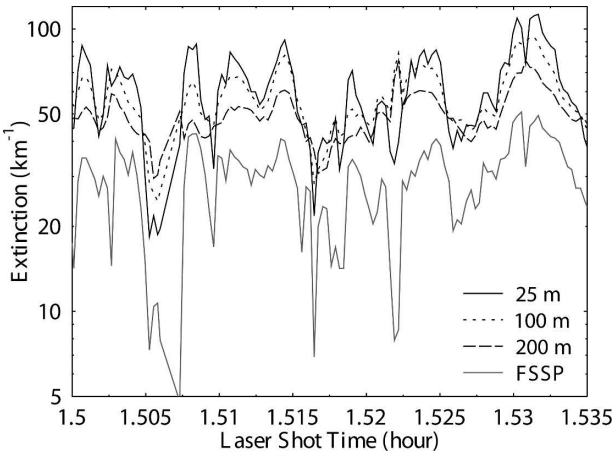

FIG. 11. Example lidar retrievals of extinction at three averaging scales indicated by the rms radius of the Gaussian weighting function. The FSSP-derived extinction is shown for comparison.

bution of thickness from 200 to 1200 m (was 200 to 1000 m), the lidar signals are simulated out to 45 μs, the laser beam divergence is 0.5°, and 4×10^7 Monte Carlo photons are simulated per location. A neural network is trained on a random half of the 400 cases to predict the cloud extinction averaged over Gaussian weighted volumes of 25-, 50-, 100-, and 200-m rms radius centered on the laser location. A separate network is trained to predict the cloud thickness and cloud relative aircraft altitude (i.e., $Z_{\text{plane}} = 0.5$ means the aircraft is at the cloud center) from the a, b, and c fit parameters for each detector. The retrieval errors are estimated using the procedure described in Evans et al. (2003) in which the rms retrieval error is calculated from the half of the 400 cases not used in the neural network training. The rms errors in volume-averaged extinction are estimated to be about 7%, and the rms errors in cloud thickness and Z_{plane} are estimated to be 80 m and 0.055, respectively. These error estimates are relative, and do not include the unknown calibration error of the lidar, which mostly affects the extinction retrievals.

Before performing the retrievals with the neural networks, laser shots with low returned signal or poor functional fits are removed. Shots with a below -28 (for photon fraction in units of $\mu s^{-1} ster^{-1} cm^{-2}$), c less than zero, or the mean absolute misfit to the function $\ln p(t) = a - b \ln(t) - ct$ exceeding 0.69 [a factor of 2 in terms of $p(t)$] are edited out. The 10-Hz lidar retrievals are averaged to 1-s sampling and merged with the FSSP extinction and aircraft position data.

An example of the in situ lidar extinction retrievals and comparison with the FSSP-derived extinction is shown in Fig. 11. The 25-m scale lidar extinction tracks the FSSP extinction quite well, although it is substantially higher. The FSSP extinction tends to have a larger range of variation, especially for narrow regions of low extinction, as the lidar averages over the small-scale variations seen by the FSSP (Baker 1992). The 100- and 200-m lidar extinctions tend to be smoother and lower than the 25-m extinctions as the larger volume sensed includes lower extinction regions at lower altitudes or above cloud top. Occasionally the 100- and 200-m lidar extinction curves are anticorrelated to the 25-m lidar and FSSP extinction curves as around 1.522 h UTC, which is presumably due to a nearby dense cloud region beyond about 50 m from the aircraft.

Figure 12 is a scatterplot of the lidar-retrieved and FSSP extinction. The R^2 correlation (fraction of variance explained) in log extinction of the points with lidar extinction greater than 10 km^{-1} is 0.837. This correlation is quite high considering that the lidar is measuring a cloud volume more than 10^{10} times larger than the FSSP probe. The offset of the lidar extinction from the FSSP extinction is a factor of 1.8, and is presumably due to the uncertainties in the lidar and the FSSP calibrations.

Table 2 shows that the correlation of the lidar and FSSP extinction declines markedly with increasing volume scale of the lidar retrieval. This correlation decrease with scale is expected as the FSSP measurement along a line becomes less representative of the cloud volume at large scales in these inhomogeneous clouds. These results indicate that the in situ lidar provides large-scale cloud information not obtainable from traditional cloud probes.

Although the single-wavelength in situ lidar inher-

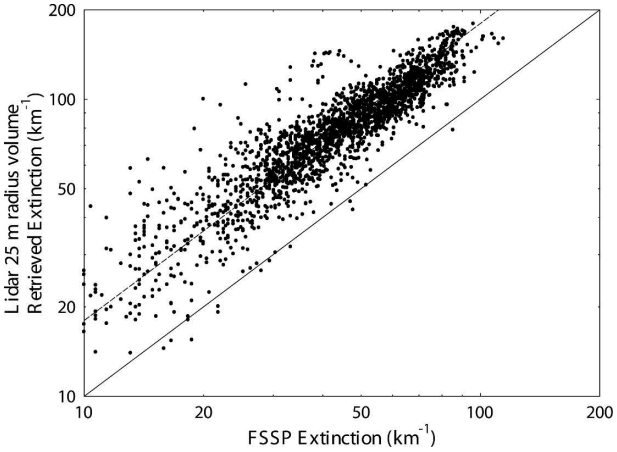

FIG. 12. A scatterplot of the lidar-retrieved extinction vs the FSSP-derived extinction. The 1:1 and 1.8:1 lines are shown.

ently measures extinction in liquid clouds, the lidar has the ability to infer LWC due to the correlation between extinction and LWC. Table 2 shows that the correlation between the lidar-retrieved extinction and the FSSP and King probe LWC is almost as high as with the FSSP extinction. The reason for this is that the correlation between FSSP LWC and extinction is quite high (R^2 = 0.925) for this marine stratus case.

One would expect higher correlation between the lidar and FSSP extinction values in regions of the cloud that are more homogeneous. To test this hypothesis the samples are divided into high and low extinction variability as measured by the lidar. The lidar extinction variability is defined as the standard deviation of the log of the retrieved extinction over 10 lidar shots. The high- and low-variability points are distinguished separately for each of 20 bins of lidar extinction (with equal number of points in each bin). Figure 13 shows the lidar-retrieved and FSSP extinction scatterplots for low and high variability. There is a small but noticeable difference in the correlation between the high- and low-variability subsets.

TABLE 2. Correlation of the in situ lidar-retrieved log extinction and the FSSP log extinction, FSSP log LWC, and King log LWC. The R^2 correlation is the fraction of the variance explained. The lidar radius is the rms radius of the Gaussian-weighted volume average. The correlation is calculated for the 2262 one-second samples with 25-m lidar extinction greater than 10 km^{-1}.

	R^2 correlation		
Lidar radius (m)	FSSP extinction	FSSP LWC	King LWC
25	0.837	0.783	0.736
50	0.788	0.752	0.717
100	0.601	0.585	0.571
200	0.399	0.405	0.400

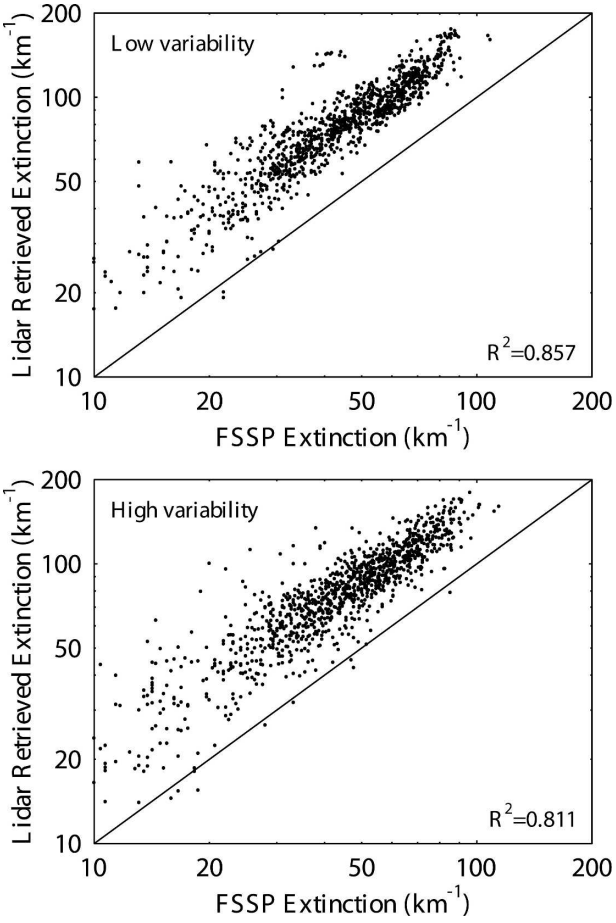

FIG. 13. Scatterplots of the lidar-retrieved 25-m scale extinction vs the FSSP-derived extinction for low and high lidar extinction variability. The R^2 correlation in log extinction is listed.

The only means available in this experiment to evaluate the lidar cloud thickness (Δz) and cloud relative altitude (Z_{plane}) retrievals are the aircraft penetrations of cloud base and top. The comparison is facilitated by deriving the lidar-retrieved cloud top and base using

$$z_{\text{top}} = z_{\text{ac}} + \Delta z(1 - Z_{\text{plane}})$$
$$z_{\text{base}} = z_{\text{ac}} - \Delta z Z_{\text{plane}}, \quad (4)$$

where z_{ac} is the aircraft altitude. Since the lidar retrievals of cloud thickness and cloud relative aircraft altitude are expected to be more reliable in denser regions away from cloud boundaries, only points with $0.15 < Z_{\text{plane}} < 0.85$ and lidar 25-m extinction greater than 60 km^{-1} (about 33 km^{-1} FSSP extinction) are used.

Figure 14 shows the lidar-retrieved cloud top and base compared with the aircraft altitude at cloud-top and -base penetrations as determined by the FSSP con-

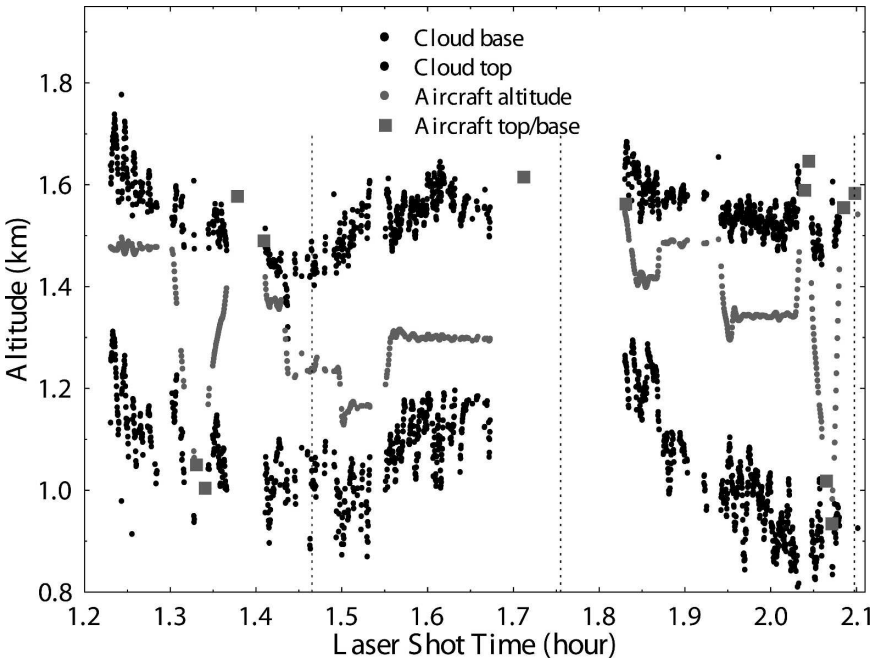

FIG. 14. Cloud-base and -top altitude derived from lidar-retrieved cloud thickness and cloud-relative altitude and aircraft altitude. Also shown are the aircraft altitude and the top and base altitudes obtained from cloud boundaries derived from the FSSP probe. The vertical dotted lines indicate the times of farthest south or north latitude.

centration. The lidar-retrieved cloud-base and -top altitude shows a consistent trend to lower altitudes to the south and higher altitudes to the north. The lidar-retrieved cloud boundary altitudes are fairly consistent independent of aircraft altitude. There is about a 100-m local variability in the lidar-retrieved cloud base and top, which is correlated with the retrieved extinction. This local variability may be partly lidar retrieval error and partly actual cloud-base and -top variability. There is reasonably good agreement between the lidar-retrieved and aircraft-derived cloud boundaries, though there is considerable variation in the aircraft-derived boundary altitudes.

5. Summary and future work

An in situ cloud lidar was designed and built at SPEC Inc. A 532-nm wavelength Nd:YAG laser sends 182-mJ pulses at a 10-Hz rate horizontally from the aircraft through an optical quality cabin window. A beam expander is used to achieve no-visual-interference eye safety at 1000 ft. The laser light scatters around the optically thick cloud and a small portion reaches the upward- and downward-viewing detectors on the opposite-side wing tip. The light enters either the daytime or nighttime set of optics for each detector. The daytime optics has a 3° field of view (FOV) and blocks the solar background with a 0.37-nm-wide interference filter. The nighttime optics uses a compound parabolic collector (Winston cone) to funnel light from a 30° FOV and 50-mm entrance aperture to the 25-mm exit aperture. The light intensity is measured with a photomultiplier tube (PMT). An electronics board for each detector converts the PMT current to voltage, amplifies, and digitizes at a 10- or 20-MHz sampling rate. The electronics achieves a single-shot dynamic range exceeding 10^6 using two 14-bit ADCs (low- and high-gain channels) and a TIA gain switch. An onboard digital signal processor controls the amplifier and ADCs and implements an automatic control system that changes the PMT gain by factors of 10 according to the peak photon return. A data system computer in the aircraft cabin sends commands to the detector electronics and records and displays the PMT current signal. The postprocessing calibration from PMT current to the photon fraction time series is done with a system equation approach that uses measured values for each relevant component (laser energy, filters, optics angular response, PMT gain, etc.).

An example from the first engineering flight of the in situ lidar illustrates that daytime operation is feasible in spite of the solar background light. Using background subtraction, the usable signal extends over three orders of magnitude and beyond 15 μs in dense cloud.

In situ lidar data are analyzed from a nighttime flight with about 1 h in inversion capped stratus off the coast of south Texas. The lidar signals clearly show the effects of radiative smoothing over distance (laser shot time), with later photon travel times being much smoother than early photon travel times. This radiative smoothing occurs because later photon travel times imply larger volumes sampled by the randomly diffusing photons. A structure function analysis quantifies how the variability in lidar signal decreases with the photon time. The radiative smoothing regime is scaling and has a steeper power-law slope (less variability at shorter distances) than the actual cloud variability.

Retrievals of extinction averaged over four volumes (radii from 25 to 200 m) and cloud thickness and cloud-relative altitude are made from the upward- and downward-viewing in situ lidar signals. The retrievals are made with neural networks trained on simulated lidar signals from stochastic 3D stratus fields. The in situ lidar-retrieved volume averaged extinction is "validated" by comparison to FSSP derived extinction. The R^2 correlation for log extinction is 0.84 for 25-m radius lidar extinction and decreases to 0.40 for 200-m radius lidar extinction. The correlation between the FSSP and 25-m lidar extinction is high, given that the lidar samples a volume more than 10^{10} times that of the FSSP. The decrease in correlation with the size of the lidar sampling volume implies that there is an increase in inhomogeneity above the 100-m scale. In situ lidar retrievals of cloud-top and -base height compare favorably with the heights determined from occasional aircraft penetrations. Given the limitations of the corroborating measurements, these comparisons are only a preliminary validation of the in situ lidar technique. We look forward to more extensive validation efforts in future deployments.

The first task for future work with the in situ lidar will be developing an accurate calibration method. Measuring the in situ lidar signal from a molecular Rayleigh scattering atmosphere was attempted, but the signal was apparently below the detection level. Molecular scattering is probably the most straightforward and accurate calibration method and may still be feasible, perhaps by pointing the detectors closer to the laser beam. Using a target of known reflectance in the laser beam could be used for calibration if the detector fields of view are scanned across the narrow target so that the angular response can be integrated.

The existing single-wavelength in situ lidar would be especially valuable for validating satellite and airborne remote sensing of optical depth in shallow clouds. The scale of the in situ lidar sampling matches the remote sensing measurements, and the difficulties of vertical integration with traditional cloud probes are avoided. Since the in situ lidar measures the most variable optical property (extinction) in warm clouds over large volumes, it would be a valuable instrument in inhomogeneous cloud-radiation closure studies. The in situ lidar would be useful in stratocumulus research for locating the aircraft vertically within the cloud and for measuring the structure on 10–100-m scales.

The in situ lidar theory could be extended to ice clouds. In optically thick clouds of either phase, diffusion theory indicates that the in situ lidar measures the scaled extinction, $(1 - g)\beta$, where β is the extinction and g is the asymmetry parameter. The existing instrument has the sensitivity to operate in cirrus of moderate to low optical depth, for which the lidar signals would contain a combination of extinction and phase function information.

In situ lidar instrumentation could be miniaturized for use on a small unmanned aerial vehicle (UAV) (Holland et al. 2001) and still provide accurate extinction retrievals in most liquid clouds. A lightweight in situ lidar would have a solid state laser, with microjoule pulse energy and thousands of pulses per second, and large area avalanche photodiode detectors. Simulations (assuming perfect calibration) indicate that a photon fraction lower limit of 10^{-13} μs^{-1} $ster^{-1}$ cm^{-2} would still provide better than 10% accuracy in volume-averaged extinction up to a radius of 100 m and extinctions down to 15 km^{-1}. This photon fraction sensitivity could be achieved for a micropulse in situ lidar with averaging times of the order of 1 s.

An exciting future instrumentation extension is the dual wavelength in situ lidar technique for measuring LWC and effective radius (Evans et al. 2003). A deuterium gas Raman shifting cell can efficiently convert the Nd:YAG fundamental to 1560.7 nm (where water droplets absorb, but molecular absorption is low). A smaller and lower-cost option is to use a KTP optical parametric oscillator (OPO) crystal to convert the Nd:YAG fundamental to a tunable wavelength greater than 1572.5 nm (e.g., Roy and Mathieu 1996). Cooled avalanche photodiodes are sensitive detectors at these wavelengths.

Acknowledgments. We gratefully acknowledge Warren Wiscombe's support of this project from its inception. Financial support was provided by NASA SBIR phase 2 contract NAS5-02111 to SPEC Inc. Financial support was also provided (for KFE) by the Environmental Sciences Division of the U.S. Department of Energy (under Grant DE-A1005-90ER61069 to NASA Goddard Space Flight Center) as part of the ARM program.

REFERENCES

Baker, B. A., 1992: Turbulent entrainment and mixing in clouds: A new observational approach. *J. Atmos. Sci.,* **49,** 387–404.

Cahalan, R. F., M. McGill, J. Kolasinski, T. Varnai, and K. Yetzer, 2005: THOR—Cloud thickness from offbeam lidar returns. *J. Atmos. Oceanic Technol.,* **22,** 605–627.

Davis, A. B., A. Marshak, R. F. Cahalan, and W. J. Wiscombe, 1997: The Landsat scale break in stratocumulus as a three-dimensional radiative transfer effect: Implications for cloud remote sensing. *J. Atmos. Sci.,* **54,** 241–260.

——, R. F. Cahalan, J. D. Spinhirne, M. J. McGill, and S. P. Love, 1999: Off-beam lidar: An emerging technique in cloud remote sensing based on radiative Green-function theory in the diffusion domain. *Phys. Chem. Earth B,* **24,** 177–185.

Evans, K. F., R. P. Lawson, P. Zmarzly, D. O'Connor, and W. J. Wiscombe, 2003: In situ cloud sensing with multiple scattering lidar: Simulations and demonstration. *J. Atmos. Oceanic Technol.,* **20,** 1505–1522.

Holland, G. J., and Coauthors, 2001: The aerosonde robotic aircraft: A new paradigm for environmental observations. *Bull. Amer. Meteor. Soc.,* **82,** 889–902.

Knollenberg, R. G., 1981: Techniques for probing cloud microstructure. *Symposium on Clouds: Their Formation, Optical Properties, and Effects,* P. V. Hobbs and A. Deepak, Eds., Academic Press, 15–91.

Love, S. P., A. B. Davis, C. Ho, and C. A. Rohde, 2001: Remote sensing of cloud thickness and liquid water content with Wide-Angle Imaging Lidar (WAIL). *Atmos. Res.,* **59–60,** 295–312.

Polonsky, I. N., S. P. Love, and A. B. Davis, 2005: Wide-angle imaging lidar deployment at the ARM southern Great Plains site: Intercomparison of cloud property retrievals. *J. Atmos. Oceanic Technol.,* **22,** 628–648.

Roy, G., and P. Mathieu, 1996: Comparison of Raman and degenerated optical parametric oscillators for a high-energy and high-repetition-rate eye-safe laser. *Opt. Eng.,* **35,** 3579–3584.

Welford, W. T., and R. Winston, 1989: *High Collection Nonimaging Optics.* Academic Press, 284 pp.